



1 **Mapping the performance of a versatile water-based**
2 **condensation particle counter (vWCPC) with COMSOL**
3 **simulation and experimental study**
4

5 Weixing Hao¹, Fan Mei^{2,*}, Susanne Hering³, Steven Spielman³, Beat Schmid²,
6 Jason Tomlinson², Yang Wang^{1,*}
7

8 ¹Department of Chemical, Environmental and Materials Engineering,
9 University of Miami, Miami, FL, 33146, USA

10 ²Pacific Northwest National Laboratory, Richland, WA, 99352, USA
11

12 ³Aerosol Dynamics Inc., Berkeley, CA, 94710, USA
13

14 *Correspondence to:* Fan Mei (fan.mei@pnnl.gov), Yang Wang (yangwang@miami.edu)



15 **Abstract.**

16 Accurate airborne aerosol instrumentation is required to determine the spatial distribution of ambient aerosol particles,
17 particularly when dealing with the complex vertical profiles and horizontal variations of atmospheric aerosols. A
18 versatile water-based condensation particle counter (vWCPC) has been developed to provide aerosol concentration
19 measurements under various environments with the advantage of reducing the health and safety concerns associated
20 with using butanol or other chemicals as the working fluid. However, the airborne deployment of vWCPCs is relatively
21 limited due to the lack of characterization of vWCPC performance at reduced pressures. Given the complex
22 combinations of operating parameters in vWCPCs, modeling studies have advantages in mapping vWCPC
23 performance.

24

25 In this work, we thoroughly investigated the performance of a laminar flow vWCPC using COMSOL Multiphysics®
26 simulation coupled with MATLAB. We compared it against a modified commercial vWCPC (vWCPC Model 3789,
27 TSI, Shoreview, MN, USA). Our simulation determined the performance of particle activation and droplet growth in
28 the vWCPC growth tube, including the supersaturation, $D_{p,ke1,0}$ (smallest size of particle that can be activated),
29 $D_{p,ke1,50}$ (particle size activated with 50% efficiency) profile, and final growth particle size D_d under wide operating
30 temperatures, inlet pressures P (0.3 – 1 atm), and growth tube geometry (diameter D and initiator length L_{ini}). The
31 effect of inlet pressure and conditioner temperature on vWCPC 3789 performance was also examined and compared
32 with laboratory experiments. The COMSOL simulation result showed that increasing the temperature difference (ΔT)
33 between conditioner temperature T_{con} and initiator T_{ini} will reduce $D_{p,ke1,0}$ and the cut-off size $D_{p,ke1,50}$ of the
34 vWCPC. In addition, lowering the temperature midpoint ($T_{mid} = \frac{T_{con} + T_{ini}}{2}$) increases the supersaturation and slightly
35 decreases the $D_{p,ke1}$. The droplet size at the end of the growth tube is not significantly dependent on raising or lowering
36 the temperature midpoint but significantly decreases at reduced inlet pressure, which indirectly alters the vWCPC
37 empirical cut-off size. Our study shows that the current simulated growth tube geometry ($D = 6.3$ mm and $L_{ini} = 30$
38 mm) is an optimized choice for current vWCPC flow and temperature settings. The current simulation can more
39 realistically represent the $D_{p,ke1}$ for 7 nm vWCPC and also achieved a good agreement with the 2 nm setting. Using
40 the new simulation approach, we provide an optimized operation setting for the 7 nm setting. This study will guide
41 further vWCPC performance optimization for applications requiring precise particle detection and atmospheric aerosol
42 monitoring.



43 **1 Introduction**

44 Aerosols, defined as any solid or liquid particles suspended in air, are one of the fundamental components of the
45 atmosphere and have a significant impact on air quality, climate change and human health (Seinfeld et al., 2016;
46 Anderson et al., 2020; Lighty et al., 2000; Pöschl, 2005; Prather et al., 2020; Li et al., 2017; Paasonen et al., 2013;
47 Darquenne, 2012). However, accurate and comprehensive monitoring of aerosol particles is challenging because
48 aerosol particle sizes and number concentrations vary widely both spatially and temporally (Davidson et al., 2005; Yu
49 and Luo, 2009; Krudysz et al., 2009). Airborne measurements and characterization, therefore, are often required to
50 capture the vertical profiles and horizontal variability of atmospheric aerosols.

51

52 In understanding the variability of atmospheric aerosol and determining the size distribution and number concentration
53 of aerosols, laminar-flow, butanol-based Condensation Particle Counters (CPCs) used in conjunction with differential
54 mobility analyzers (DMAs) can provide real-time measurements of airborne particles and are widely used by
55 effectively exploiting the working principle of condensation growth (Hermann et al., 2007; Kangasluoma and Attoui,
56 2019; Mordas et al., 2008; Sem, 2002; Wiedensohlet et al., 1997). However, conventional butanol CPCs face
57 difficulties in characterizing particles below 3 nm in size. In addition, health and safety risks, such as the odor,
58 flammability and toxicity of the butanol, are an issue for many deployments in offices, homes, aircraft, and other
59 inhabited locations. These limitations have led directly to researchers designing advanced aerosol instruments that can
60 be more widely used in both atmospheric environments and laboratory studies.

61

62 In 2005, Hering and Stolzenburg (2005) developed a continuous-flow, water-based laminar condensation particle
63 counter (WCPC) (Hering et al., 2005; Hering and Stolzenburg, 2005), which uses distilled water as the working fluid
64 to avoid the health and safety concerns. It was also found to have comparable performance to butanol-based CPCs in
65 previous studies (Biswas et al., 2005; Franklin et al., 2010; Iida et al., 2008; Kupc et al., 2013; Liu et al., 2006; Mordas
66 et al., 2008). A modified version of the WCPC featuring an additional new moderator section has been developed
67 (Hering et al., 2014). With this new moderated approach, the initiator provides water vapor for particle activation
68 while the moderator provides distance and time for particle growth. This improved water CPC achieves the same peak
69 supersaturation and similar droplet growth while reducing the water vapor, particle loss, and side effects of heating
70 the flow in the earlier version of WCPC. Furthermore, a versatile WCPC was then developed capable of particle
71 detection near 1 nm without using a filtered sheath flow. The operating temperatures can also be adjusted in accordance
72 with the cut-point desired (Hering et al., 2017).

73

74 Since water-based CPCs have comparable performance to butanol-based CPCs while also offering the advantage of
75 avoiding health and safety risks, it is desirable to explore advanced water-based CPCs in a broader range of
76 environmental and energy applications. To improve the detection performance of the vWCPC, we need to identify the
77 effects of operational factors and geometry. However, the limited analysis of relevant temperature and geometric
78 parameters in the vWCPC makes it challenging to control condensational growth conditions. In addition, the inlet
79 pressure effect is another critical factor affecting the detection efficiency of vWCPCs. The potential of using vWCPC



80 for airborne deployment or other lower pressure monitoring has not been fully explored. Mei et al. (2021) found that
81 the counting efficiency of the vWCPC 3789 operated at the factory settings decreased with decreasing the operating
82 pressure, particularly at operating pressures below 700 hPa. However, determining how to reduce the lower detection
83 limit under various ambient pressures also needs to be investigated.

84

85 Due to the complex matrix of geometry, operating temperature, and inlet pressure parameters in vWCPCs, modeling
86 studies are advantageous in determining and optimizing the detection efficiency of vWCPCs. The Graetz model was
87 first used by Stolzenburg (1988) to examine the detection of ultrafine particles in CPCs. In recent years, COMSOL
88 Multiphysics® has been widely used to simulate coupled heat, mass, and momentum transfer problems associated
89 with complex geometries in CPCs. Moreover, COMSOL has advantages in interfacing with post-processing software
90 such as MATLAB™. A series of parametric analyses for butanol CPCs were simulated using COMSOL to investigate
91 the performance of particle activation and droplet growth (Hao et al., 2021; Attoui, 2018; Kangasluoma et al., 2015;
92 Barmounis et al., 2018; Thomas et al., 2018). Our previous work (Hao et al., 2021) first demonstrated that the
93 COMSOL results neglecting the temperature dependence of vapor thermodynamic properties and axial diffusion,
94 agree with the Graetz solution used by Stolzenburg (1988). Considering temperature dependence of vapor
95 thermodynamic properties and axial diffusion can generate more accurate results that can guide the optimization of
96 CPC designs. Previous research using COMSOL to examine vWCPC performance has been limited. Bian et al. (2020)
97 compared two-stage and three-stage operating temperature methods for growth tubes and parameters such as flow rate
98 and temperature difference to obtain the ideal activation and final growth sizes. Mei et al. (2021) used COMSOL
99 aiding to examine how inlet pressure affects particle activation in the vWCPCs. However, the lack of thorough and
100 systematic examination of vWCPC performance using COMSOL leaves it unclear on how well the vWCPC will
101 perform in multiple complex research areas and applications, such as at reduced atmospheric pressure levels.

102

103 In this study, we thoroughly determined the saturation profile, activation efficiency, and droplet growth for varying
104 airborne operations through numerical simulation of laminar flow vWCPC in COMSOL and experimental validation
105 of a commercial vWCPC (TSI Model 3789). By mapping vWCPC performance in the modeling, the effects of various
106 operational factors, such as inlet pressures (0.3 - 1 atm), growth tube diameter and initiator length, and temperature
107 gradients on particle activation and droplet growth, were investigated. In addition, detailed modeling methods are
108 outlined below. The detection efficiency was also examined in the experimental and COMSOL modeling work. The
109 results of this study will guide further optimization of the performance of vWCPCs for accurate detection of particles
110 and atmospheric aerosol measurement applications.

111



112 2 Methods

113 2.1 Numerical simulation

114 2.1.1 COMSOL setup

115 The finite element COMSOL simulation software (COMSOL Multiphysics 5.3a, COMSOL Inc, Stockholm, Sweden)
116 can handle a variety of fields including, but not limited to, electromagnetics, fluid dynamics, heat transfer, chemical
117 reactions, and structural mechanics. Here, a two-dimensional axisymmetric model is developed to simulate fluid flow
118 in a cylindrical tube. The heat, momentum, and mass transfer equations are solved for incompressible parabolic flow.
119 This COMSOL model follows the three-stage tube of the versatile water-based CPC (TSI Inc, Shoreview, MN, USA)
120 described by Hering et al. (2017), which consists of a fully developed laminar flow tube that can be separated into a
121 cool-wall conditioner region, a warm-wall initiator region, and a cool-wall moderator region, where r is the radial
122 coordinate of the tube diameter and z is the axial coordinate of the tube length (**Fig. 1a**). At the inlet of the conditioner
123 tube, sampled aerosols are fed and saturated with water vapor before entering the initiator region. The manufacturer
124 provides two default cut-off diameter settings: 2 and 7 nm configurations based on the characteristics introduced by
125 Kangasluoma et al. (2017). This study used the 7 nm configuration as an example to demonstrate the simulation
126 mapping effort. The methodology can also be used for other targeted cut-off sizes. The tube diameter (D) is 6.3 mm,
127 the conditioner length (L_{con}) is 73 mm, the initiator length (L_{ini}) is 30 mm, and the moderator length (L_{mod}) is 73 mm.
128 The default settings are (**Table 1**): the conditioner temperature (T_{con}) is 30 °C, the initiator temperature (T_{ini}) is 59 °C,
129 and the moderator temperature (T_{mod}) is 10 °C. The aerosol flow rate (Q_v) is 0.3 L min⁻¹. The relative humidity (RH)
130 of inlet flow is set at 20%, and the water vapor is assumed to be saturated at the wall. The inlet pressure (P) is 1 atm.
131 To investigate how the vWCPC performance depends on these parameters, we simulate a wide range of values for
132 mapping the vWCPC geometry, working temperature conditions, and inlet pressure, as discussed in Section 2.1.4 for
133 the tasks in this study.

134

135 In this COMSOL model, the coupled heat transfer and fluid flow are first solved by the conjugate heat transfer module,
136 and then the mass transfer of the water vapor is solved based on the obtained temperature and flow field. Lastly, the
137 particles are introduced from the inlet of the vWCPC and are considered diluted species that follow the convective
138 diffusion equation in the simulation, which is numerically solved to calculate the temperature, supersaturation, and
139 water vapor concentration profiles (**Fig. 1**). Regarding the initial and boundary value settings, the inflow temperature
140 is set to an ambient temperature of 25 °C, and wall temperature is set to the default factory settings described above
141 and changed as the experimental conditions changed for mapping performance. The simulated temperature and
142 concentration fields are then imported into MATLAB™ R2022b (The MathWorks, Inc., Natick, MA, USA) and
143 interpolated at any given point in the r - z plane. COMSOL Multiphysics 5.3a with MATLAB allows us to adjust
144 geometry, modify physics settings, perform parametric studies, control solvers, and post-process the results.

145



146 2.1.2 Theory of particle activation

147 Particle activation is key to the evaluation of CPC performance. Particle activation within the vWCPC depends on the
148 degree of supersaturation, namely the saturation ratio (S) of water vapor, which is the ratio of the partial pressure of
149 the water vapor (p) to the saturation vapor pressure of the water vapor (p_s) for the given flow temperature (T),
150 calculated by

$$S = \frac{p}{p_s} \quad (1)$$

151 The spatial profile of S within the vWCPC allows us to calculate the Kelvin effect, the homogeneous nucleation, and
152 further condensational particle growth, as discussed in Section 2.1.3. The Kelvin effect is dependent upon
153 thermodynamic principles and described as the Kelvin equivalent size ($D_{p,ke}$), the minimum diameter of a particle
154 that can be activated for condensation growth. It is determined by water surface tension (σ), water molecular volume
155 (v_m), the Boltzmann constant (k), temperature (T) and the saturation ratio (S) calculated at each location within the
156 initiator,

$$D_{p,ke} = \frac{4\sigma v_m}{kT \ln(S)} \quad (2)$$

157 The Kelvin equivalent size is inversely proportional to the distribution of saturation ratio, where the greater the
158 saturation ratio, the smaller the size of the particles that can be activated. In other words, the smaller the particle, the
159 higher the degree of supersaturation required to activate growth. When particle size (D_p) is above $D_{p,ke}$, the particle
160 can be successfully activated and grown by water vapor condensation, while when D_p is below $D_{p,ke}$, the particles
161 cannot be activated. **Fig. 1b - 1e** show examples of saturation ratio, Kelvin equivalent size, water vapor concentration,
162 and temperature profiles within the simulated geometry at the default temperature condition of $T_{con} = 30$ °C, $T_{ini} = 59$
163 °C, $T_{mod} = 10$ °C, respectively.

164

165 It is worth noting that $D_{p,ke}$ varies at different locations of the initiator due to the spatial variation of temperature,
166 surface tension and saturation ratio. We observed the potential particle activation in the moderator by simulation
167 results. However, only the Kelvin equivalent size in the initiator was considered in this work. Although the particles
168 were activated in the moderator, particle detection was unlikely due to droplet growth being the dominant water vapor
169 sink in the initiator. Thus, in reality, the actual supersaturation in the moderator may be different, and the activation
170 of smaller particles will be hindered by droplet growth (Hering et al., 2014; Hering et al., 2017). Note that the $D_{p,ke}$ in
171 the conditioner region is blank in color due to no particles being activated in this region ($S \leq 1$). Particles near the
172 wall of the initiator, where there is a lower S , are more difficult to activate due to the larger $D_{p,ke}$. This difference can
173 be explained by the water mass and heat diffusivity differences. As the colder, water-saturated flow passes through
174 the growth tube, the mass transport of water vapor is faster than the heating of the flow from the wall because the mass
175 diffusivity of water vapor is higher than the thermal diffusivity of air, producing a maximum supersaturation of water
176 vapor at the centerline of the tube. As a result, the seed particles entering near the centerline of the growth tube are
177 activated in the warmer initiator. One comparison of the saturation ratio and Kelvin equivalent size along the centerline
178 ($r = 0$) is shown in **Fig. S1a and S1b**. We observed the appearance of a double-peaked saturation ratio curve. Again,



179 only the Kelvin equivalent size in the initiator was considered in this work due to insufficient water vapor and droplet
180 growth in the moderator. Note that our calculations do not include the solute effects, and we assume wettable insoluble
181 particles in the modeling.

182

183 The activation efficiency of particles with a size of D_p in vWCPC is derived using an approach similar to our previous
184 work (Hao et al., 2021), which is calculated by the ratio of the number concentration of the activated particles over
185 the total particle number concentration in the growth tube. The activation efficiency is calculated as

$$\eta_{\text{act}} = \frac{\int_0^{R_{\text{act}}} 2\pi r w N dr}{Q_v N_0} \quad (3)$$

186 where w is the velocity along the axial direction, N is the concentration of particles, both at the axial location of $z =$
187 Z_{act} . R_{act} is the maximum radius of the contour corresponding to $D_{p,\text{kel}} = D_p$. N_0 is the particle concentration at the
188 inlet of the conditioner. Q_v is the flow rate through the vWCPC. An example of activation efficiency as a function of
189 particle diameter D_p can be found in **Fig. S1c**. Note that the calculation of the activation efficiency in Eq. (3) does not
190 consider the diffusion loss of the particles in the conditioner. Since this model does not have sheath flow that
191 minimizes the diffusion losses and constrains the aerosols to the high supersaturation region, the activation efficiency
192 cannot reach 100%. On the activation curve, there are two points of interest: minimum activated size, $D_{p,\text{kel},0}$ (the
193 smallest size of particle that can be activated in the initiator), and 50% cut-off size, $D_{p,\text{kel},50}$ (the size of a particle with
194 50% activation efficiency extracted from the activation efficiency curve). $D_{p,\text{kel},50}$ is essential to the performance of
195 CPCs because it determines the general particle size range in which the CPC can confidently measure. $D_{p,\text{kel},50}$ can
196 be used as the representative of particle activation efficiency performance. Furthermore, note that negligible
197 homogeneous nucleation occurs in the growth tube of the initiator and moderator under all tested conditions in this
198 study, which means the total nucleation rate is equal to or less than one particle per second (1 s^{-1}).

199

200 2.1.3 Theory of droplet growth

201 Once the particles are activated, their condensational growth along their trajectories in the initiator region was
202 simulated by numerically solving two coupled differential equations in MATLABTM. First, the evolution of droplet
203 diameter (D_p) can be governed by (Seinfeld and Pandis, 2008; Wang et al., 2017)

$$\frac{dD_p}{dt} = \frac{4D'_v M (C - C_d)}{\rho D_p} \quad (5)$$

204 where M and ρ represent the molecular weight and density of water, D'_v represents the modified diffusivity of the
205 water vapor accounting for the non-continuum effect of the particles and is given by $D'_v = D_v \left[1 + \frac{2D_v}{\alpha_c D_p} \left(\frac{2\pi M}{RT} \right)^{1/2} \right]^{-1}$,
206 where D_v is the diffusivity of the water vapor, and α_c is the mass accommodation coefficient of water and is assumed
207 as 1. C_d represents the equilibrium water concentration at the surface of the growth droplets and is given by $C_d =$



208 $C_s(T_d) \exp\left(\frac{4\sigma M}{\rho R T_d D_p}\right)$, where C_s is saturation water concentration, T_d is the droplet surface temperature, which is
209 governed by

$$\frac{dT_d}{dt} = \frac{3}{c_p \rho D_p} \left(H_{\text{vap}} \rho \frac{dD_p}{dt} - 4k'_g \frac{(T_d - T)}{D_p} \right) \quad (6)$$

210 where c_p , ρ , and H_{vap} are the heat capacity, density, and heat of vaporization of water. k'_g represents the modified
211 thermal conductivity of air accounting for the non-continuum effects in heat transfer and is calculated as $k'_g =$
212 $k_g \left[1 + \frac{2k_g}{\alpha_T D_p \rho_g c_{p,g}} \left(\frac{2\pi M_g}{RT} \right)^{1/2} \right]^{-1}$, where M_g , ρ_g , $c_{p,g}$, and k_g are the molecular weight, density, heat capacity, and
213 thermal conductivity of air. α_T is the thermal accommodation coefficient and was assumed to be 1 (Seinfeld and
214 Pandis, 2008; Wang et al., 2017).

215

216 In the simulation of droplet growth, the Brownian motion of the particles inside the conditioner before activation is
217 neglected. Since there is also no electric field inside the conditioner, we assume that the particles move axially along
218 the vWCPC with a velocity of w . Therefore, Eqs. (5) and (6) can be converted to a function of axial location using
219 $w = dz/dt$, and the droplet size and droplet surface temperature at the end of the moderator ($z = L_{\text{ini}} + L_{\text{mod}}$) can be
220 calculated. To determine the final droplet growth size at the outlet of the moderator, the condensational growth of 8
221 nm particles as seed particles was studied along the centerline ($r = 0$) of the growth tube in this work. An example of
222 droplet growth size as a function of distance along the axis of the tube for the default temperature condition of $T_{\text{con}} =$
223 30°C , $T_{\text{ini}} = 59^\circ\text{C}$, $T_{\text{mod}} = 10^\circ\text{C}$ can be found in **Fig. S1d**. Note that in this simulation, we do not consider the
224 increase in the equilibrium vapor pressure due to warming of the flow from condensational heat release, which would
225 further reduce the droplet growth.

226

227 2.1.4 Simulation plan

228 **Table 1** summarizes the operating temperatures, inlet pressures, and geometric parameters for each simulation task
229 characterizing the vWCPC in this study. In Task 1, we first conducted two matrix combinations of absolute conditioner
230 and initiator operating temperatures, with an interval of 5°C in each region, for a total of nine different combinations.
231 Task 2 investigates how raising or lowering the temperature midpoints (T_{mid}), the average value between the
232 conditioner temperature and initiator temperature ($\frac{T_{\text{con}} + T_{\text{ini}}}{2}$) affects particle activation and droplet growth. In
233 addition, different inlet pressures are also included when comparing different temperature midpoints. Task 3 examines
234 the effect of inlet pressure by comparing the default temperature of 30°C and the conditioner temperature of 27°C .
235 Tasks 4 and 5 further test how the vWCPC geometry, including tube diameter D , and initiator length L_{ini} , affects the
236 performance of the vWCPC. These simulations reveal optimal working conditions and effects for the influence of
237 each parameter.

238



239 2.2 Experimental measurement

240 The modified vWCPC 3789 (TSI Inc, Shoreview, MN, USA) was tested in this study. Operating flow, temperatures
241 and geometry can be found in Section 2.1.1 and our previous study (Mei et al., 2021). Two methods were used to
242 generate the test aerosol: an atomizer coupled with a furnace; and a glowing wire generator (GWG). Ammonium
243 sulfate (AS) has been commonly used for CPC characterization and was the tested material used in this study (Hering
244 et al., 2014; Kangasluoma et al., 2017). It was dissolved into deionized water for aerosol generation using atomization
245 techniques. To increase the aerosol number concentration for particles less than 30 nm, polydisperse AS aerosols were
246 also passed through a tube furnace generator (Lindberg/Blue, Thermal Scientific, TX, USA) to shift the size
247 distribution to a smaller size. A lab-built GWG was also used to generate aerosol particles in size range between 2.5
248 – 16 nm. More details about the generator can be found in Attoui (2022). Using the low-pressure testing setup shown
249 in **Fig. S2**, the counting efficiency of a vWCPC 3789 was measured between 0.5-0.9 atm for AS particles of 3 – 20
250 nm (mobility diameter) and NiCr oxidants of 2.5 -16 nm. The aerosol concentrations in this test were maintained in
251 the range of $2 \times 10^4 - 4 \times 10^4 \text{ cm}^{-3}$. During the testing, the temperature variations in the conditioner and moderator were
252 less than 0.5 °C, and the initiator temperature had a variation of 1 °C. The y-axis error bar indicates the standard
253 deviation of the counting efficiency averaged over ~ 5 min of sampling time at a 1 Hz sampling rate.

254

255 3 Results and discussion

256 3.1 Comparisons of temperature-dependent particle activation and droplet growth performance

257 Selection of appropriate operating temperatures in CPCs is essential because the supersaturation is significantly
258 temperature dependent, which affects particle activation and further droplet growth. In addition, the temperature
259 difference between different regions in CPCs is an important factor in controlling supersaturation. For this reason, the
260 minimum activation size for butanol-based CPCs is significantly impacted by the temperature difference between the
261 saturator and condenser and the raising or lowering of the temperature midpoints, as has been demonstrated by many
262 previous studies (Hermann and Wiedensohler, 2001; Kangasluoma and Attoui, 2019; Barmponis et al., 2018; Kuang
263 et al., 2012). The results showed that in the butanol-based CPCs, the greater the temperature difference between the
264 saturator and condenser, the higher the degree of supersaturation, and the smaller particle could be activated.

265

266 The numerical COMSOL model was used to compare operating temperature-dependent particle activation and droplet
267 growth performance in the vWCPC, including minimum activated size ($D_{p,ke1,0}$), 50% cut-off size ($D_{p,ke1,50}$), and final
268 growth particle size at the outlet of the moderator along the centerline ($r = 0$) (D_d), as shown in **Fig. 2**. Previous studies
269 confirmed that the centerline saturation rate is insensitive to the moderator wall temperature (Hering et al., 2014; Bian
270 et al., 2020). Thus, this study investigated moderator temperature (T_{mod}) at the constant of 10 °C, conditioner
271 temperature (T_{con}) at the range of 25 – 35 °C, initiator temperature (T_{ini}) at the range of 55 – 65 °C. Note that conditions
272 that can lead to a lower $D_{p,ke1,50}$ value and larger droplet growth size are favored for improving the performance of
273 the vWCPC.

274



275 Firstly, in order to compare the effect of the conditioner temperature T_{con} , we increased T_{con} from 25 °C to 35 °C
276 while maintaining the same initiator temperature T_{ini} and moderator temperature T_{mod} , $D_{\text{p,ke1,0}}$ increased significantly
277 by 5.21, 3.32, and 2.27 nm at the initiator temperature T_{ini} of 55, 60, and 65 °C, respectively, and $D_{\text{p,ke1,50}}$ increased
278 significantly by 6.65, 4.16, and 2.75 nm at the initiator temperature T_{ini} of 55, 60, and 65 °C, respectively. The final
279 droplet size D_{d} decreased by approximately 1 μm at all the initiator temperature T_{ini} of 55, 60, 65 °C. The lower
280 conditioner temperature provided higher saturation ratios in the initiator and more water vapor for particle growth,
281 which is also consistent with the previous growth tube simulation (Bian et al., 2020; Mei et al., 2021). Secondly, the
282 initiator temperature T_{ini} was increased from 55 °C to 65 °C while maintaining the same conditioner temperature T_{con}
283 and moderator temperature T_{mod} , $D_{\text{p,ke1,0}}$ was decreased by 1.90, 3.74, and 4.87 nm at the conditioner temperature
284 T_{con} of 25, 30, and 35 °C, respectively, $D_{\text{p,ke1,50}}$ was decreased significantly by 2.32, 3.74, and 6.21 nm at the
285 conditioner temperature T_{con} of 25, 30, and 35 °C, respectively, and D_{d} was increased by 2.9 μm at all the conditioner
286 temperature T_{con} of 25, 30, and 35 °C.

287

288 By comparing all combinations, we can find that the activated size becomes smaller as the temperature difference
289 between T_{con} and T_{ini} increases, indicating that the temperature differences between the conditioner and initiator
290 dominate the particle activation. After comparing the temperature differences, we conclude that the higher the
291 temperature between these two regions, the better the particle activation. However, in the actual operation of the CPC,
292 one also needs to ensure that the self-nucleation in the growth tube is minimized ($<1 \text{ s}^{-1}$) so that the CPC does not
293 report false particle counting. The homogeneous nucleation rate is less than 10^{-8} s^{-1} at all tested conditions, meaning
294 that the temperatures can be further adjusted to optimize particle activation and droplet growth. Moreover, D_{d} is the
295 greatest, with a maximum size of 12.20 μm , at the temperature setting of 25–65–10 °C among all these temperature
296 conditions. We also found that the effect of the initiator temperature on droplet growth was greater than that of the
297 conditioner temperature. Thus, the following section examines the effect of temperature midpoint on the vWCPC
298 performance.

299

300 3.2 Effect of temperature midpoint on particle activation and droplet growth performance

301 In addition to temperature difference, lowering the temperature midpoint was also found to cause higher
302 supersaturation. However, there is limited research on how the performance of the vWCPC changes under various
303 temperature midpoints and especially under different inlet pressures, which will be important for applications such as
304 atmospheric airborne deployment and environmental monitoring at elevated locations. Here, we compared the particle
305 activation and droplet growth performance for three different temperature midpoints (40 °C, 43 °C, and 46 °C) of
306 conditioner temperature (from 24 °C to 30 °C) and initiator temperature (56 °C to 62 °C) at a wide range of inlet
307 pressures from 0.3 atm to 1 atm, as shown in Fig. 3. The temperature difference ΔT between the conditioner and the
308 initiator was kept constant at 32 °C. The moderator temperature remained constant at 10 °C in all simulations.

309



310 Results show that the minimum activated size $D_{p,ke1,0}$ decreases from 5.15 nm to 4.96 nm, and the 50% cut-off size
311 $D_{p,ke1,50}$ decreases from 5.88 nm to 5.65 nm as the temperature midpoint decreases from 46 °C to 40 °C, as shown in
312 **Fig. 3a and 3b**. Thus, a slight control of the minimum activation size can be achieved by lowering the temperature
313 midpoint. Higher supersaturation can explain this slight decrease in the initiator, which also agrees with the previous
314 growth tube WCPC simulation (Bian et al., 2020). On the other hand, a slight increase of 0.07, 0.1, and 0.14 nm occurs
315 in $D_{p,ke1,0}$, and negligible change in $D_{p,ke1,50}$ by reducing the inlet pressure from 1 to 0.3 atm under three temperature
316 midpoints of 40 °C, 43 °C, and 46 °C. This slight increase is due to a low peak supersaturation caused by the decrease
317 in inlet pressure. Since water vapor transport is faster than heat transport, the decrease in pressure affects the location
318 of the peak supersaturation, whereas the degree of the supersaturation does not change significantly.

319

320 In **Fig. 3c**, we show that the droplet growth is not significantly dependent on raising or lowering the temperature
321 midpoint. By lowering the temperature midpoint by 6 °C, D_d becomes smaller by approximately 14%. When studying
322 the effect of inlet pressure on the D_d , unlike $D_{p,ke1,0}$ and $D_{p,ke1,50}$, D_d decreases substantially from 1 to 0.3 atm, by
323 approximately 45%. Limited by the optical chamber design of the commercial vWCPC, the droplets smaller than 8
324 μm may not gain sufficient pulse signal to get counted. Thus, when operating under lower inlet pressure, the apparent
325 cut-off size of vWCPC may increase and needs to be further determined. The reduced pressure strongly affects the
326 final droplet growth size, likely due to the faster water vapor and heat transport at reduced pressure. The thermal and
327 mass diffusivity is inversely proportional to the pressure in the growth tube, resulting in insufficient time for droplet
328 growth. In addition, we found that with the lower inlet pressure, the final droplet size reduced more notably. For
329 example, D_d decreased from 10.6 to 10.4 μm (by 0.2 μm) as pressure reduced from 1.0 to 0.9 atm, while D_d decreased
330 from 7.2 to 6.1 μm (by 1.1 μm) as pressure reduced from 0.4 to 0.3 atm. The difference can be explained by the
331 competition between heat and water vapor transport. The mass transport of water vapor is faster than the heating flow
332 from the wall because the mass diffusivity of water vapor is higher than the thermal diffusivity of air. Therefore, by
333 reducing the inlet pressure, water vapor transport becomes even faster than heat transfer due to the water vapor
334 diffusivity and air thermal diffusivity being inversely proportional to the pressure, further shortening the time for
335 particle growth at high supersaturation. This observation demonstrates for the first time how the final droplet size is
336 affected by raising or lowering temperature midpoints at standard and various reduced inlet pressure conditions in the
337 vWCPC.

338

339 **3.3 Effect of inlet operation pressure on particle activation and droplet growth performance**

340 With the advantages of safe, eco-friendly and readily available distilled water as working fluid in the vWCPC,
341 applying the vWCPC in various inlet pressures will expand broader applications such as atmospheric airborne aerosol
342 measurements. Here, we examined the effect of inlet pressure on minimum activated size, $D_{p,ke1,0}$, 50% cut-off size,
343 $D_{p,ke1,50}$, and final growth particle size at the outlet of the moderator along the centerline ($r = 0$), D_d from 0.3 to 1 atm
344 for two different temperature settings: the conditioner, initiator, and moderator temperatures were 30, 59, and 10 °C
345 and 27, 59, and 10 °C in **Fig. 4**.



346
347 **Figs. 4a and 4b** show $D_{p,ke1,0}$ and $D_{p,ke1,50}$ as a function of inlet pressure, relatively greater (2 - 3%) $D_{p,ke1,0}$ was
348 observed at reduced inlet pressures at both conditioner temperatures of 27 °C and 30 °C. This increase is because the
349 supersaturation value at reduced pressure is lower than the saturation profile under standard conditions. We also found
350 that the saturation profile peaked earlier, closer to the entrance of the initiator in the low-pressure condition. In
351 addition, greater $D_{p,ke1,50}$ is observed at reduced inlet pressures due to the reduction of the saturation peak at both
352 conditioner temperatures of 27 °C and 30 °C. Again, the difference at reduced inlet pressure can be explained by the
353 competition from heat transfer and water vapor transport, as discussed in Section 3.2. For this reason, greater $D_{p,ke1,50}$
354 was observed at reduced inlet pressures. This reduction of saturation peaks is also associated with the growing droplet
355 size decreasing with the decrease in the operating pressure. Again, lowering the conditioner temperature while
356 maintaining the same temperature difference between the initiator and the moderator provided higher saturation ratios
357 in the initiator over all pressure ranges.

358
359 **Fig. 4c** shows the final droplet size as a function of inlet pressure. When the conditioner temperature is 27 or 30 °C, a
360 lower final droplet size (~ 40 % reduction in the droplet size) was observed at a reduced inlet pressure of 0.3 atm,
361 indicating insufficient droplet growth happens at low-pressure conditions, which is consistent with the previous study
362 that insufficient droplet growth becomes more significant under low-pressure operation (Mei et al., 2021).

363
364 Furthermore, in addition to showing consistent results with the previous study (Mei et al., 2021), our simulations
365 enhance guidance for aircraft applications under extreme conditions, which can be achieved by simulating low
366 atmospheric pressure at 0.3 atm. As shown in Section 3.5, by comparing with experimental results, our simulations
367 can provide more accurate estimates of particle activation and droplet growth to guide vWCPC for low-pressure
368 applications.

369

370 **3.4 Effect of tube diameter and initiator length on particle activation and droplet growth performance**

371 The geometry in CPCs also impacts the CPC activation performance and particle growth due to the changed
372 supersaturation and temperature profile in the tube, as discussed in previous studies (Hao et al., 2021; Hering et al.,
373 2014). Here, we examined how the tube diameter D and the length of initiator L_{ini} in the vWCPC may affect the
374 minimum activated size, $D_{p,ke1,0}$, 50% cut-off size, $D_{p,ke1,50}$, and final growth particle size at the outlet of the moderator
375 along the centerline ($r = 0$), D_d under default temperature $T_{con} - T_{ini} - T_{mod}$ of 30–59–10 °C, standard inlet pressure
376 and reduced pressure of 0.5 atm using the numerical COMSOL model. Again, one needs to note that conditions that
377 can lead to a lower $D_{p,ke1,0}$ and $D_{p,ke1,50}$ value and larger droplet growth size are favored for improving the performance
378 of the vWCPC.

379

380 We examined four values of D from 4 to 8 mm, and five values of L_{ini} from 10 to 50 mm, shown in **Fig. 5** and **Fig. 6**,
381 respectively. The results indicate that a smaller D can slightly decrease in $D_{p,ke1,0}$ approximately 0.03 nm, while no



382 noticeable changes on $D_{p,ke1,50}$ at the standard pressure (**Figs. 5a and 5b**). By reducing the tube diameter, the flow
383 speed in the tube increases under the same flow rate, reducing the residence time of the condensed water vapor. This
384 reduction in residence time suppresses homogeneous nucleation in the initiator. Unlike our previous study on CPCs
385 (Hao et al., 2021), the homogeneous nucleation rate is minimal in vWCPC and has no impact on the temperature
386 difference compared to butanol-based CPCs. For this reason, this suppressed homogeneous nucleation has limited
387 effects on $D_{p,ke1,0}$ and $D_{p,ke1,50}$. However, the increase of the flow speed will significantly limit the time for droplet
388 growth, as will be discussed later. At the reduced pressure of 0.5 atm, a smaller D can slightly decrease in
389 $D_{p,ke1,0}$ approximately 0.08 nm, and a slight decrease of approximately 0.03 nm on $D_{p,ke1,50}$ (**Figs. 5a and 5b**). Overall,
390 the reduction in pressure plays a more critical role in negatively impacting CPC performance for relatively large tube
391 diameters. Note that buoyancy effects (Roberts and Nenes, 2005) may be critical for large temperature differences if
392 the tube diameter is too large, which is not discussed in the study.

393

394 On the other hand, we found that reducing L_{ini} leads to limited effects on $D_{p,ke1,0}$ and $D_{p,ke1,50}$, except for the shortest
395 initiator length of 10 mm at the standard pressure (**Figs. 6a and 6b**). The effect of these relatively long initiator lengths
396 is limited because the degree of supersaturation is determined by the absolute temperature of the tube flow. The
397 temperature difference did not change in the standard pressure and reduced pressure, leaving both $D_{p,ke1,0}$ and $D_{p,ke1,50}$
398 unchanged. However, at the initiator length of 10 mm, $D_{p,ke1,0}$ and $D_{p,ke1,50}$ increase significantly due to insufficient
399 water vapor diffusion before passing through the next moderator region, resulting in a lower peak supersaturation
400 along the centerline than for longer initiators operating at the same temperature (Hering et al., 2014). At reduced
401 pressure, $D_{p,ke1,0}$ and $D_{p,ke1,50}$ have no noticeable changes at all tested initiator lengths, however, this is due to the
402 sufficient diffusion of water vapor, from which the water transport is faster than at the standard pressure. Again, if the
403 initiator is longer, the difference in peak supersaturation will be negligible, while the peak temperature along the
404 centerline and the amount of added water vapor will be higher. Thus, for relatively short initiators, such as 20 mm
405 used in the simulation, one can provide all the necessary water vapor to create the same peak supersaturation as for
406 the longer initiators. However, the droplet growth size will be smaller (**Fig. 6c**), mainly due to the shorter growth time
407 discussed later.

408

409 With regard to the performance of particle growth, an increased D and an increased L_{ini} are beneficial for improving
410 the performance of particle growth in vWCPC at both standard and reduced pressure (**Figs. 5c and 6c**). An increased
411 D implies a decrease in the flow velocity through the high saturation region, greatly increasing the time for particle
412 growth and contributing to the sufficient growth of the particles. **Fig. 5c** shows that the final droplet sizes increase
413 significantly from 6.72 μm to 13.88 μm when D is increased from 4 mm to 8 mm at the standard pressure and increase
414 from 4.92 to 10.78 μm at the reduced pressure of 0.5 atm. The final droplet size is found to be 2 – 3 μm smaller than
415 the standard pressure at the reduced pressure. Similarly, a longer L_{ini} also leads to a larger droplet growth size. The
416 final droplet size increases from 8.66 μm to 11.26 μm when L_{ini} is increased from 10 mm to 50 mm at the standard
417 pressure and from 7.40 to 8.29 μm at the reduced pressure of 0.5 atm (**Fig. 6c**). This increase is likely due to the longer
418 growth time of the longer initiator. Also, we found that the final droplet size increases much faster at shorter initiator



419 lengths than at lengths above 20 mm, which tells us that the droplet size is more susceptible to the effects of initiator
420 length below 20 mm. This difference also means that having a longer length does not further enhance the final size of
421 the particle growth.

422

423 In addition to the performance of particle activation, it is crucial to evaluate the droplet growth performance of
424 complex geometries in the vWCPC. The time that allows the activated particle to grow in the initiator and moderator
425 is an important droplet growth kinetics assumption, representing the vWCPC performance of droplet growth. We use
426 t_g to represent allowed particle growth time, approximated with Eq. (7).

$$t_g \sim D^2 L^* / Q_v \quad (7)$$

427 where L^* indicates the length of the initiator and moderator beyond the point of activation. This equation can explain
428 that the residence time is impacted more by the change in tube diameter than the initiator length. The allowed particle
429 growth time as a function of final growth particle size at the outlet of the moderator along the centerline ($r = 0$), D_d is
430 shown in **Fig. S3**. The longer the allowed particle growth time, the larger the droplet growth size. Based on this droplet
431 growth time shown, the vWCPC geometry of D and L_{ini} are not independent variables if we consider the droplet
432 growth for further particle detection.

433

434 3.5 Experimental measurement validation of detection efficiency

435 Experimental validation is essential for simulation work in terms of the accuracy of the simulation model and the
436 correctness of the underlying trends. Furthermore, validation and good agreement will provide well-guided approaches
437 for future applications. Therefore, we compare the experimental and simulation results of the counting efficiency and
438 detection efficiency of vWCPC for two configurations of 2 nm and 7 nm at different conditioner and initiator
439 temperature settings and different low-pressure conditions in **Fig. 7**.

440

441 As the experimental results in a previous study (Mei et al., 2021) are shown in **Fig. 7a**, the counting efficiency of
442 vWCPC 3789 varied with different working pressures (500, 700 and 910 hPa) when the conditioner temperature is 27
443 °C, the initiator temperature is 59 °C, and the moderator temperature is 10 °C. The results indicate that the counting
444 efficiency slightly decreases with the decrease in the operating pressure of 500, 700 and 900 hPa, which shows the
445 same trend in **Fig. 7b**. In addition, the cut-off size in both experimental and simulation results are in the range of 5 -
446 7 nm, which is also an acceptable range within error when compared to commercial vWCPC detection efficiency.

447

448 **Fig. 7c** and **7d** compare the counting efficiency and detection efficiency versus particle size from experimental and
449 simulation results under initiator temperatures of 75 and 90°C and pressure of 910 and 500 hPa for the 2 nm
450 configuration. As expected, the detection efficiency of both experimental and simulated results is lower at the
451 temperature $T_{con} - T_{ini} - T_{mod}$ of 7-75-10 °C at a lower pressure (at 500 hPa). When the temperature $T_{con} - T_{ini} - T_{mod}$
452 is 7-90-10 °C, the higher detection efficiency is seen, and the effect of inlet pressure becomes insignificant. However,
453 it is not feasible to maintain 90 °C when operating under lower pressure, such as 500 hPa. Thus, the default 2 nm



454 setting in vWCPC can only be operated near sea level. One should note that although we do not present many
455 simulations for the 2 nm configuration, what we learned from the modeling results with the 7 nm setting will guide
456 future simulations with the 2 nm setting.

457

458 By comparing with counting efficiency curves, the present simulations can more realistically represent the $D_{p,ke1}$ for
459 7 nm vWCPC, which also achieved a good agreement with the 2 nm setting. Thus, from the merits of the results of
460 this work, we can find that this work not only provides guidance for 7 nm, but this trend can also help guide one for
461 other desired cut-off sizes.

462

463 **4 Conclusions**

464 This study evaluated the particle activation and droplet growth performance of a commercial versatile water CPC
465 using COMSOL in combination with MATLAB data processing. In addition, validation experiments on the detection
466 efficiency of the commercially modified vWCPC (TSI 3789) agreed with the simulation work. Increasing the
467 temperature difference between T_{con} and T_{in} and lowering the temperature midpoint can enhance particle activation
468 at both standard and reduced ambient pressure conditions. However, the lack of droplet growth becomes more
469 significant under low-pressure operations, which might affect the apparent counting efficiency of the vWCPC due to
470 the limited measurable size range of the optical chamber. Additionally, reducing the diameter of the growth tube
471 slightly improved particle activation without enhancing the droplet growth, while increasing the initiator length had a
472 limited effect on improving the performance of the vWCPC at both standard and reduced pressure.

473

474 This simulation realistically represents the $D_{p,ke1}$ for 7 nm vWCPC and shows that the current growth tube geometry
475 is an optimized choice for aerosol measurements. This study will guide further vWCPC performance optimization for
476 applications requiring precise particle detection and atmospheric aerosol monitoring. Furthermore, the developed
477 simulation capability provides a vital tool for the aerosol community to understand the effects of temperature and
478 pressure on vWCPC behavior. The knowledge gained will guide the field deployment of vWCPC on the ground level
479 and airborne measurements. Thus, several future experimental studies will be carried out to investigate the
480 performance of the vWCPC.

481

482 **Data availability**

483 The vWCPC data in the study are available upon request to Fan Mei (fan.mei@pnnl.gov).

484

485 **Author contributions**

486 WH, FM, and YW designed the research. FM carried out the measurements. WH led the simulation and data analyses.
487 WH led the writing, with significant input from FM and YW as well as further input from all other authors. SH, SS,
488 BS, and JT provided suggestions on the revision.

489



490 **Competing interests**

491 Susanne Hering has a commercial interest in the success of the vWCPC instrument.

492

493 **Acknowledgments**

494 Hao and Wang are partially supported by NSF award 2132655.

495

496 **References**

- 497 Anderson, E. L., Turnham, P., Griffin, J. R., and Clarke, C. C.: Consideration of the aerosol transmission for
498 COVID - 19 and public health, *Risk Analysis*, 40, 902-907, 2020.
- 499 Attoui, M.: Activation of sub 2 nm singly charged particles with butanol vapors in a boosted 3776 TSI CPC, *J*
500 *Aerosol Sci*, 126, 47-57, 2018.
- 501 Attoui, M.: Mobility distributions of Sub 5 nm singly self-charged water soluble and non-soluble particles from a
502 heated NiCr wire in clean dry air, *Aerosol Sci Tech*, 56, 859-868, 2022.
- 503 Barmounis, K., Ranjithkumar, A., Schmidt-Ott, A., Attoui, M., and Biskos, G.: Enhancing the detection efficiency
504 of condensation particle counters for sub-2 nm particles, *J Aerosol Sci*, 117, 44-53, 2018.
- 505 Bian, J., Gui, H., Xie, Z., Yu, T., Wei, X., Wang, W., and Liu, J.: Simulation of three-stage operating temperature
506 for supersaturation water-based condensational growth tube, *Journal of Environmental Sciences*, 90, 275-285, 2020.
- 507 Darquenne, C.: Aerosol deposition in health and disease, *Journal of aerosol medicine and pulmonary drug delivery*,
508 25, 140-147, 2012.
- 509 Davidson, C. I., Phalen, R. F., and Solomon, P. A.: Airborne particulate matter and human health: a review, *Aerosol*
510 *Sci Tech*, 39, 737-749, 2005.
- 511 Hao, W. X., Stolzenburg, M., Attoui, M., Zhang, J. S., and Wang, Y.: Optimizing the activation efficiency of sub-3
512 nm particles in a laminar flow condensation particle counter: Model simulation, *J Aerosol Sci*, 158, 2021.
- 513 Hering, S. V. and Stolzenburg, M. R.: A method for particle size amplification by water condensation in a laminar,
514 thermally diffusive flow, *Aerosol Sci Tech*, 39, 428-436, 2005.
- 515 Hering, S. V., Spielman, S. R., and Lewis, G. S.: Moderated, water-based, condensational particle growth in a
516 laminar flow, *Aerosol Sci Tech*, 48, 401-408, 2014.
- 517 Hering, S. V., Stolzenburg, M. R., Quant, F. R., Oberreit, D. R., and Keady, P. B.: A laminar-flow, water-based
518 condensation particle counter (WCPC), *Aerosol Sci Tech*, 39, 659-672, 2005.
- 519 Hering, S. V., Lewis, G. S., Spielman, S. R., Eiguren-Fernandez, A., Kreisberg, N. M., Kuang, C., and Attoui, M.:
520 Detection near 1-nm with a laminar-flow, water-based condensation particle counter, *Aerosol Sci Tech*, 51, 354-362,
521 2017.
- 522 Hermann, M. and Wiedensohler, A.: Counting efficiency of condensation particle counters at low-pressures with
523 illustrative data from the upper troposphere, *J Aerosol Sci*, 32, 975-991, 2001.
- 524 Hermann, M., Wehner, B., Bischof, O., Han, H.-S., Krinke, T., Liu, W., Zerrath, A., and Wiedensohler, A.: Particle
525 counting efficiencies of new TSI condensation particle counters, *J Aerosol Sci*, 38, 674-682, 2007.



- 526 Kangasluoma, J. and Attoui, M.: Review of sub-3 nm condensation particle counters, calibrations, and cluster
527 generation methods, *Aerosol Sci Tech*, 53, 1277-1310, 2019.
- 528 Kangasluoma, J., Ahonen, L., Attoui, M., Vuollekoski, H., Kulmala, M., and Petäjä, T.: Sub-3 nm particle detection
529 with commercial TSI 3772 and Airmodus A20 fine condensation particle counters, *Aerosol Sci Tech*, 49, 674-681,
530 2015.
- 531 Kangasluoma, J., Hering, S., Picard, D., Lewis, G., Enroth, J., Korhonen, F., Kulmala, M., Sellegri, K., Attoui, M.,
532 and Petäjä, T.: Characterization of three new condensation particle counters for sub-3 nm particle detection during
533 the Helsinki CPC workshop: the ADI versatile water CPC, TSI 3777 nano enhancer and boosted TSI 3010,
534 *Atmospheric Measurement Techniques*, 10, 2271-2281, 2017.
- 535 Krudysz, M., Moore, K., Geller, M., Sioutas, C., and Froines, J.: Intra-community spatial variability of particulate
536 matter size distributions in Southern California/Los Angeles, *Atmospheric Chemistry and Physics*, 9, 1061-1075,
537 2009.
- 538 Kuang, C., Chen, M., McMurry, P. H., and Wang, J.: Modification of laminar flow ultrafine condensation particle
539 counters for the enhanced detection of 1 nm condensation nuclei, *Aerosol Sci Tech*, 46, 309-315, 2012.
- 540 Li, Z., Guo, J., Ding, A., Liao, H., Liu, J., Sun, Y., Wang, T., Xue, H., Zhang, H., and Zhu, B.: Aerosol and
541 boundary-layer interactions and impact on air quality, *National Science Review*, 4, 810-833, 2017.
- 542 Lighty, J. S., Veranth, J. M., and Sarofim, A. F.: Combustion aerosols: factors governing their size and composition
543 and implications to human health, *Journal of the Air & Waste Management Association*, 50, 1565-1618, 2000.
- 544 Mei, F., Spielman, S., Hering, S., Wang, J., Pekour, M. S., Lewis, G., Schmid, B., Tomlinson, J., and Havlicek, M.:
545 Simulation-aided characterization of a versatile water-based condensation particle counter for atmospheric airborne
546 research, *Atmospheric Measurement Techniques*, 14, 7329-7340, 2021.
- 547 Mordas, G., Petäjä, T., and Ulevičius, V.: Optimisation of the operation regimes for the water-based condensation
548 particle counter, *Lithuanian Journal of Physics*, 52, 2012.
- 549 Mordas, G., Manninen, H., Petäjä, T., Aalto, P., Hämeri, K., and Kulmala, M.: On operation of the ultra-fine water-
550 based CPC TSI 3786 and comparison with other TSI models (TSI 3776, TSI 3772, TSI 3025, TSI 3010, TSI 3007),
551 *Aerosol Sci Tech*, 42, 152-158, 2008.
- 552 Paasonen, P., Asmi, A., Petäjä, T., Kajos, M. K., Äijälä, M., Junninen, H., Holst, T., Abbatt, J. P., Arneth, A., and
553 Birmili, W.: Warming-induced increase in aerosol number concentration likely to moderate climate change, *Nature*
554 *Geoscience*, 6, 438-442, 2013.
- 555 Pöschl, U.: Atmospheric aerosols: composition, transformation, climate and health effects, *Angewandte Chemie*
556 *International Edition*, 44, 7520-7540, 2005.
- 557 Prather, K. A., Marr, L. C., Schooley, R. T., McDiarmid, M. A., Wilson, M. E., and Milton, D. K.: Airborne
558 transmission of SARS-CoV-2, *Science*, 370, 303-304, 2020.
- 559 Roberts, G. and Nenes, A.: A continuous-flow streamwise thermal-gradient CCN chamber for atmospheric
560 measurements, *Aerosol Sci Tech*, 39, 206-221, 2005.
- 561 Seinfeld, J. and Pandis, S.: *Atmospheric chemistry and physics*. 1997, New York, 2008.



562 Seinfeld, J. H., Bretherton, C., Carslaw, K. S., Coe, H., DeMott, P. J., Dunlea, E. J., Feingold, G., Ghan, S.,
563 Guenther, A. B., and Kahn, R.: Improving our fundamental understanding of the role of aerosol– cloud interactions
564 in the climate system, *Proceedings of the National Academy of Sciences*, 113, 5781-5790, 2016.
565 Sem, G. J.: Design and performance characteristics of three continuous-flow condensation particle counters: a
566 summary, *Atmospheric research*, 62, 267-294, 2002.
567 Stolzenburg, M. R.: An ultrafine aerosol size distribution measuring system, University of Minnesota 1988.
568 Thomas, J. M., Chen, X., Maißer, A., and Hogan Jr, C. J.: Differential heat and mass transfer rate influences on the
569 activation efficiency of laminar flow condensation particle counters, *International Journal of Heat and Mass*
570 *Transfer*, 127, 740-750, 2018.
571 Wang, J., Pikridas, M., Spielman, S. R., and Pinterich, T.: A fast integrated mobility spectrometer for rapid
572 measurement of sub-micrometer aerosol size distribution, Part I: Design and model evaluation, *J Aerosol Sci*, 108,
573 44-55, 2017.
574 Wiedensohlet, A., Orsini, D., Covert, D., Coffmann, D., Cantrell, W., Havlicek, M., Brechtel, F., Russell, L., Weber,
575 R., and Gras, J.: Intercomparison study of the size-dependent counting efficiency of 26 condensation particle
576 counters, *Aerosol Sci Tech*, 27, 224-242, 1997.
577 Yu, F. and Luo, G.: Simulation of particle size distribution with a global aerosol model: contribution of nucleation to
578 aerosol and CCN number concentrations, *Atmospheric Chemistry and Physics*, 9, 7691-7710, 2009.
579



580 **Table of Nomenclature**

- 581 c : Molecular concentration of the water vapor [mol m^{-3}]
582 C_d : Equilibrium water concentration at the surface of the growth droplets [mol m^{-3}]
583 C_s : Saturation water concentration [mol m^{-3}]
584 c_p : Heat capacity of the water [$\text{J K}^{-1} \text{kg}^{-1}$]
585 $c_{p,g}$: Heat capacity of air [$\text{J K}^{-1} \text{kg}^{-1}$]
586 D_v : Diffusivity of the water vapor [$\text{m}^2 \text{s}^{-1}$]
587 D'_v : Modified diffusivity of the water vapor [$\text{m}^2 \text{s}^{-1}$]
588 D : Diameter of the growth tube in vWCPC [m]
589 D_p : Particle size [m]
590 D_d : Final growth droplet size in vWCPC [m]
591 $D_{p,ke1}$: Size of particle that can be activated according to the Kelvin equation [m]
592 $D_{p,ke1,0}$: Smallest size of particle that can be activated in the vWCPC [m]
593 $D_{p,ke1,50}$: Size of particle that has a 50% activation efficiency [m]
594 H_{vap} : Heat of vaporization of water [J kg^{-1}]
595 k : Boltzmann constant, 1.38×10^{-23} [J K^{-1}]
596 k_g : Thermal conductivity of air [$\text{W m}^{-1} \text{K}^{-1}$]
597 k'_g : Modified thermal conductivity of air [$\text{W m}^{-1} \text{K}^{-1}$]
598 L_{con} : Length of the conditioner [m]
599 L_{ini} : Length of the initiator [m]
600 L_{mod} : Length of the moderator [m]
601 L^* : Length of the initiator and moderator beyond the point of activation [m]
602 m : Molecular mass of water [kg]
603 M : Molecular weight of water [kg mol^{-1}]
604 M_g : Molecular weight of air [kg mol^{-1}]
605 n : Molecular concentration of the water vapor [molecules m^{-3}]
606 N : Concentration of the particles at the axial location of $z = Z_{\text{act}}$ [particles m^{-3}]
607 N_0 : Concentration of particles at the inlet of the conditioner [particles m^{-3}]
608 p : Partial pressure of the water vapor [Pa]
609 p_s : Saturation vapor pressure of the water vapor [Pa]
610 P : Inlet pressure in vWCPC [Pa]
611 Q_v : Flow rate through the vWCPC [$\text{m}^3 \text{s}^{-1}$]
612 r : Radial coordinate of the tube diameter of the vWCPC [m or as otherwise explicitly designated]
613 R : Gas constant [$\text{J mol}^{-1} \text{K}^{-1}$]
614 R_{act} : Maximum radius of the contour corresponding to $D_{p,ke1} = D_p$ [m]
615 S : Saturation ratio [1]



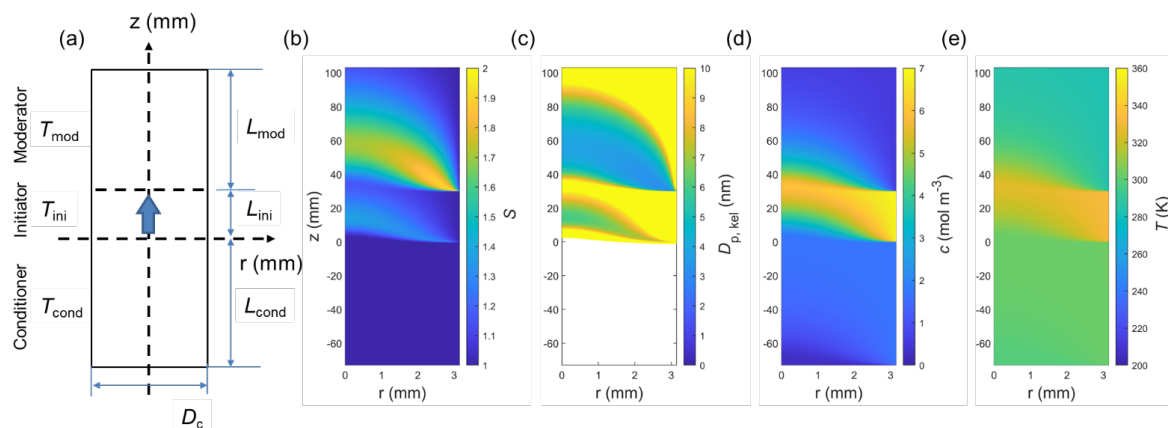
- 616 t : Allowed particle growth time [s]
617 T : Flow temperature in the CPC [K]
618 T_{con} : Conditioner temperature [K]
619 T_{ini} : Initiator temperature [K]
620 T_{mid} : Temperature midpoint corresponding to $\frac{T_{\text{con}}+T_{\text{ini}}}{2}$ [K]
621 T_{mod} : Moderator temperature [K]
622 T_{d} : Droplet surface temperature [K]
623 v_{m} : Molecular volume of the water vapor [m^3]
624 w : Velocity along the axial direction in the vWCPC [m s^{-1}]
625 z : Axial coordinate of the tube length of the vWCPC [m or as otherwise explicitly designated]
626 Z_{act} : Axial location corresponding to $r = R_{\text{act}}$ [m]
627 α_{c} : Mass accommodation coefficient of water [1]
628 α_{T} : Thermal accommodation coefficient of air [1]
629 η_{act} : Activation efficiency [1]
630 ρ : Density of water [kg m^{-3}]
631 ρ_{g} : Density of air [kg m^{-3}]
632 σ : Surface tension of water [N m^{-1}]
633 ΔT : Temperature difference between conditioner temperature and initiator temperature [K]



634 **Table 1. Parameters of vWCPC for different simulation tasks. Note that the default settings of VWPC are: the conditioner**
635 **temperature (T_{con}) is 30 °C, the initiator temperature (T_{ini}) is 59 °C, and the moderator temperature (T_{mod}) is 10 °C. The**
636 **aerosol flow rate (Q_v) is 0.3 L min⁻¹. The relative humidity (RH) of inlet flow is set at 20%, and the water vapor is assumed**
637 **to be saturated at the wall. The inlet pressure (P) is 1 atm.**

Task	T_{con} (°C) - T_{ini} (°C)	T_{mod} (°C)	T_{mid} (°C)	P (atm)	D (mm)	L_{ini} (mm)
1	(25, 30, 35) - (55, 60, 65)	10	-	1	6.3	30
2	24 - 56, 27 - 59, 30 - 62	10	40, 43, 46	0.3 - 1	6.3	30
3	27 - 59, 30 - 59	10	-	0.3 - 1	6.3	30
4	30 - 59	10	-	0.5, 1	4, 5, 6.3, 8	30
5	30 - 59	10	-	0.5, 1	6.3	10, 20, 30, 40, 50

638



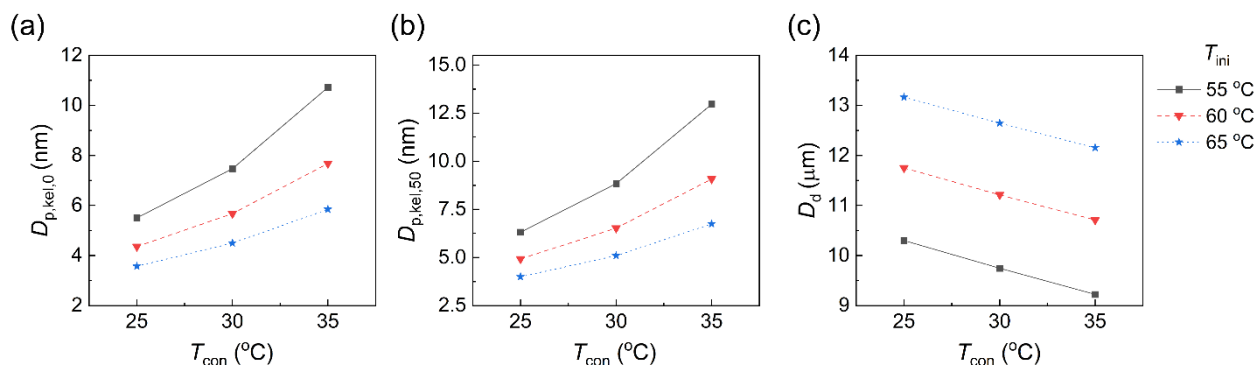
639

640

641 **Figure 1. Geometry of vWCPC used in COMSOL simulation and spatial distribution of saturation ratio and Kelvin**
642 **equivalent size under 30–59–10 °C temperature setting. (a) Geometry of the vWCPC used in COMSOL simulation, (b)**
643 **Spatial distribution of saturation ratio (S , color contour plot), (c) Spatial distribution of Kelvin equivalent size ($D_{p,kel}$, color**
644 **contour plot), (d) Spatial distribution of water vapor concentration (c , color contour plot), and (e) Spatial distribution of**
645 **temperature (T , color contour plot). Note that the color of $D_{p,kel}$ in the conditioner region is blank because no particles are**
646 **activated in this region.**

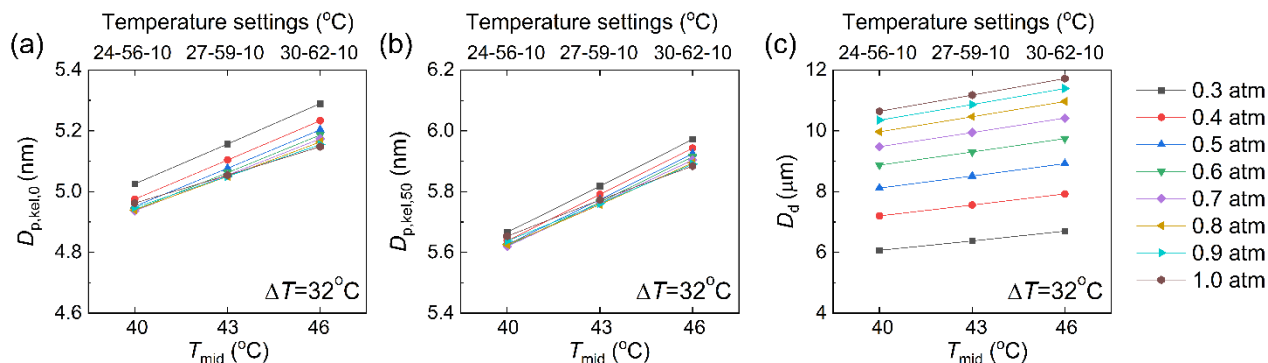


647



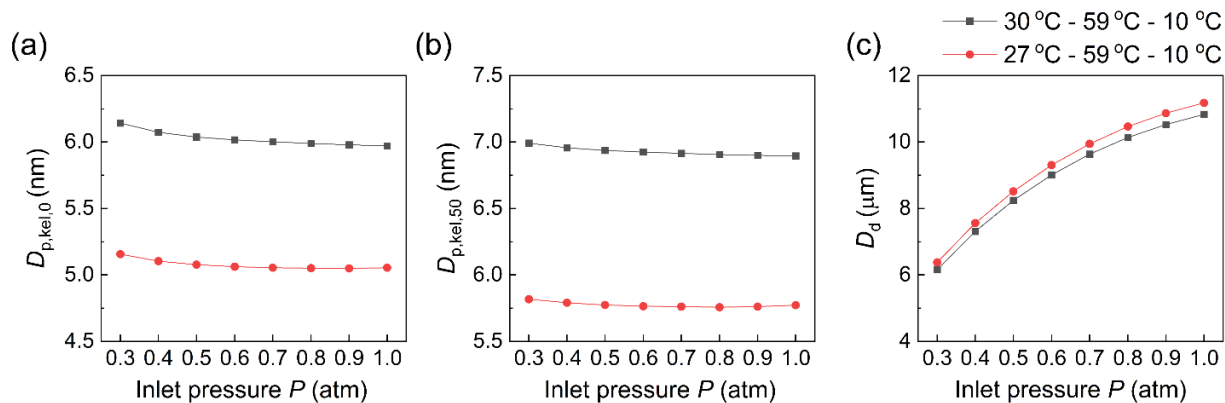
648

649 **Figure 2. Effect of conditioner (T_{con}) and initiator temperature (T_{ini}) on (a) minimum activated size, $D_{p,ke1,0}$, (b) 50%**
650 **cut-off size, $D_{p,ke1,50}$, and (c) final growth particle size at the outlet of the moderator along the centerline ($r = 0$), D_d .**
651 **The condensational growth of 15 nm particles was tested as seed particles.**



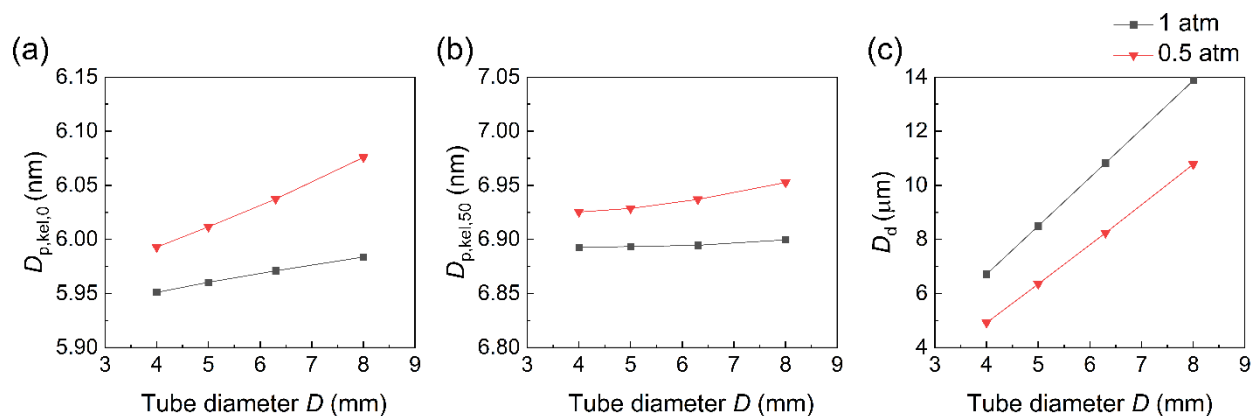
652

653 **Figure 3. Effect of temperature midpoints at 40 °C, 43 °C, and 46 °C at $T_{con}-T_{ini}-T_{mod}$ of 24–56–10 °C, 27–59–10 °C**
 654 **and 30–62–10 °C with a constant temperature difference of 32 °C on (a) minimum activated size, $D_{p,ke1,0}$, (b) 50% cut-**
 655 **off size, $D_{p,ke1,50}$, and (c) final growth particle size at the outlet of the moderator along the centerline ($r = 0$), D_d . The**
 656 **condensational growth of 8 nm particles was tested as seed particles.**



657

658 **Figure 4.** Effect of inlet operation pressure at $T_{\text{con}}-T_{\text{ini}}-T_{\text{mod}}$ of 27–59–10 °C and 30–59–10 °C on (a) minimum
659 activated size, $D_{p,ke1,0}$, (b) 50% cut-off size, $D_{p,ke1,50}$, and (c) final growth particle size at the outlet of the moderator
660 along the centerline ($r = 0$), D_d . The condensational growth of 8 nm particles was tested as seed particles.



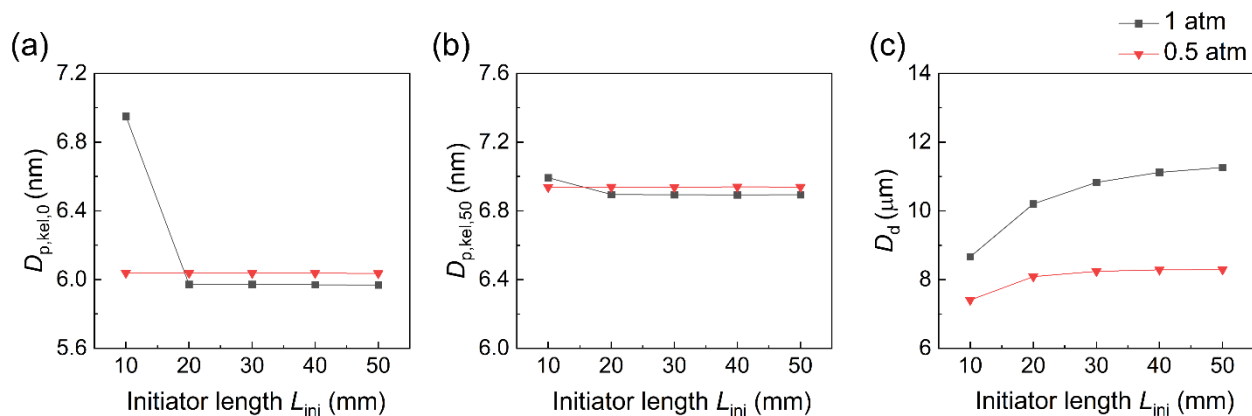
661

662

663

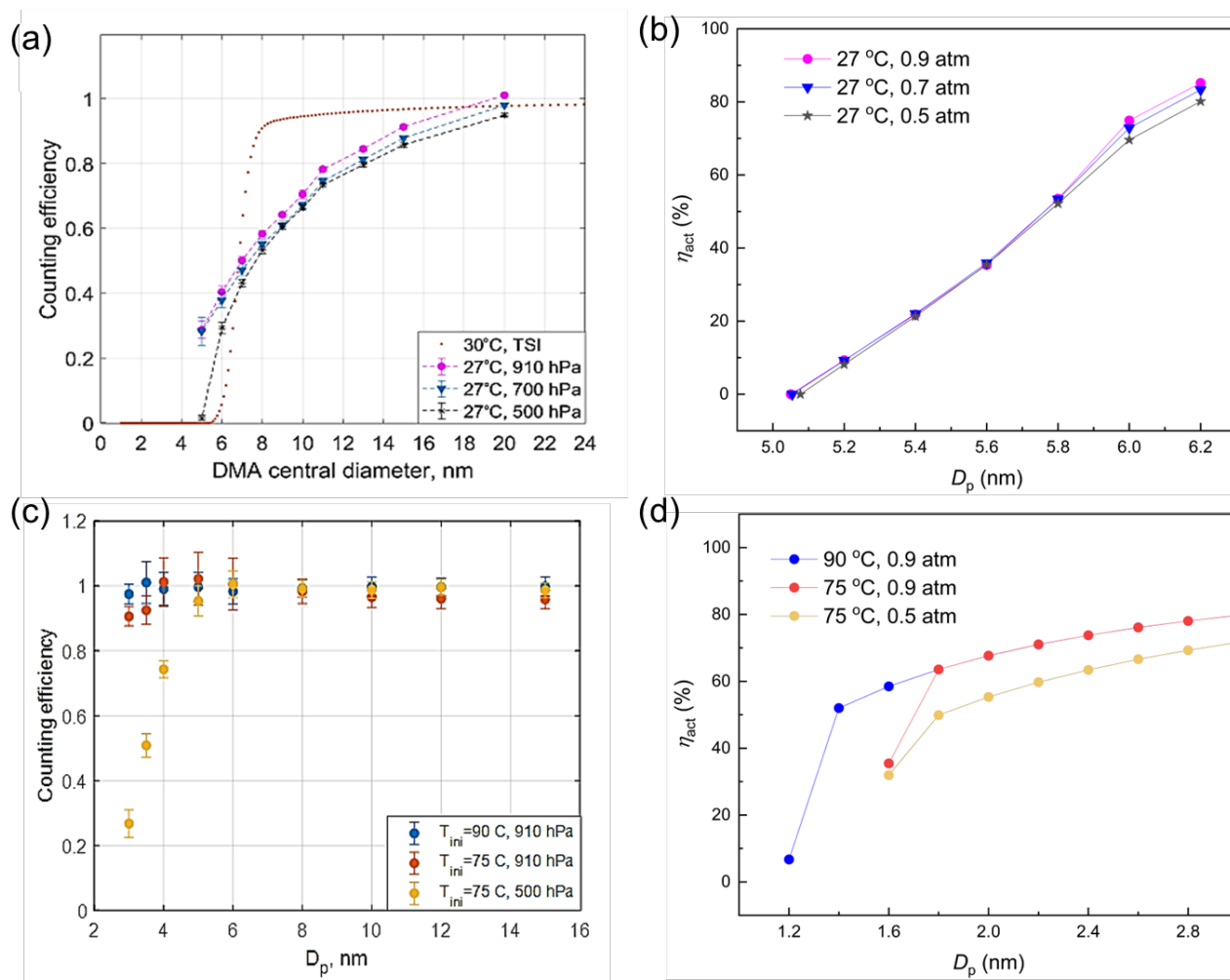
664

Figure 5. Effect of tube diameter (D) at 0.5 atm and 1 atm on (a) minimum activated size, $D_{p,ke1,0}$, (b) 50% cut-off size, $D_{p,ke1,50}$, and (c) final growth particle size at the outlet of the moderator along the centerline ($r = 0$), D_d . The condensational growth of 8 nm particles was tested as seed particles.



665

666 **Figure 6. Effect of initiator length (L_{ini}) at 0.5 atm and 1 atm on (a) minimum activated size, $D_{p,ke1,0}$, (b) 50% cut-off**
667 **size, $D_{p,ke1,50}$, and (c) final growth particle size at the outlet of the moderator along the centerline ($r = 0$), D_d . The**
668 **condensational growth of 8 nm particles was tested as seed particles.**



669

670 **Figure 7. vWCPC operation validation: (a) the counting efficiency of experimental results as a function of particle size**
671 **under the conditioner temperature of 27 °C and pressure of 910, 700, and 500 hPa for the 7 nm configuration, (b) the**
672 **detection efficiency of simulation results as a function of particle size under the conditioner temperature of 27 °C and**
673 **pressure of 0.9, 0.7, and 0.5 atm for the 7 nm configuration, (c) the detection efficiency of experimental results as a**
674 **function of particle size under initiator temperatures of 75 and 90°C and pressure of 910 and 500 hPa for the 2 nm**
675 **configuration, and (d) the detection efficiency of simulation results as a function of particle size under initiator**
676 **temperatures of 75 and 90°C and pressure of 0.9 and 0.5 atm for the 2 nm configuration.**